JOURNAL OF MATERIALS SCIENCE **40** (2005) 1229–1235

Crack growth in a new nickel-based superalloy at elevated temperature

Part II *Finite element analysis of crack growth*

L.-G. ZHAO, J. TONG*
Department of Mechanical and Design Engineering, University of Portsmouth, Anglesea Road, Anglesea Building, Portsmouth PO1 3DJ, UK

Crack growth at elevated temperature has been simulated using the finite element method for sustained and cyclic loading conditions, representative of time-dependent and time-independent crack growth. Elastic-creep (EC) and elastic-plastic-creep (EPC) models have been used to simulate the crack growth under sustained loads at 650 and 725°C. Crack mouth opening displacements as well as the evolution of the inelastic zones due to creep and plasticity have been obtained. Elastic-plastic finite element analysis has been carried out to simulate the crack growth under cyclic load using a constitutive model. Fatigue crack growth was simulated for plane stress, plane strain and generalized plane strain loading conditions. The influence of plasticity on the effective crack driving force was also examined.

Creep damage was found to be very limited at both temperatures for this alloy. Plasticity-induced crack closure was found to be absent in plane strain or generalized plane strain conditions, overestimated in plane stress loading conditions by the conventional compliance method.

1. Introduction

Crack growth at elevated temperature has been reported in a new fine-grained nickel-based superalloy under a variety of loading conditions at 650 and 725°C [1]. A mixture of time and cycle dependent crack growth has been observed for base frequencies over 0.01 Hz while time dependent crack growth was found in long dwell and sustained load cases. To understand the fundamental mechanisms of crack growth at elevated temperature, material constitutive models have been utilized in the simulation of the crack growth behaviour under typical loading conditions.

Time-dependent crack growth is usually simulated using elastic-secondary creep models [2–4], where the crack growth may be either creep ductile or creep brittle, depending on the extent of creep deformation that accompanies the crack growth. Significant creep deformation occurs in creep-ductile materials where the crack may be considered nearly stationary within the field of an expanding creep zone. The asymptotic stress field is of Hutchinson-Rice-Rosagren (HRR) type [2], and in the limiting case, relates uniquely to a crack tip line integral [3]. An instantaneous stress-power dissipation rate [5] is used to characterize the crack growth rate. For creep-brittle materials, however, creep deformation tends to be limited and the crack growth rate is comparable to the expansion rate of the creep zone at the crack tip. In such cases, the stress intensity factor K is considered more appropriate, particularly at steady-state crack growth stage. For a cracked-body undergoing creep deformation, the load-line deflection rate is often used as a measure of material characteristics. For $\dot{V}_C/\dot{V} \geq 0.8$, where $\dot{V}_C$ is the load-line deflection rate due to creep and $\dot{V}$ is the total deflection rate, the material is regarded as creep ductile [6] while $\dot{V}_C/\dot{V} \ll 1$ indicates creep brittle. For the alloy used in the present study, creep curves have been obtained from conventional creep tests at 650 and 725°C [7]. These curves will be used to obtain the parameters in elastic-creep (EC) and elastic-plastic-creep (EPC) models to simulate the time-dependent crack growth. The load-line deflection rate and the creep zone expansion rate will be examined to determine the material creep characteristics. This information will form the base for the selection of an appropriate parameter in the characterization of time-dependent crack growth in Part III.

For time-independent fatigue crack growth, crack closure has been reported as the complication giving rise to amorphous crack growth behaviour. The concept of effective stress intensity factor range has been used to improve the correlation between the fatigue crack growth rate and the stress intensity factor range. It is known, however, that material characteristics may have a profound influence on the simulated crack growth pattern, hence the crack closure characteristics [8–10], although early work on crack closure has largely based on

*Author to whom all correspondence should be addressed.

simplified material models. In this work, a full constitutive model will be used to simulate advancing fatigue cracks under plane stress, plane strain and generalised plane strain conditions. The role of plasticity-induced crack closure will be critically examined. This information will again be used in the characterization of time-independent fatigue crack growth in Part III.

2. Modelling of crack growth under sustained load

2.1. Numerical procedures

2.1.1. The theory

For small strain deformation, the time-dependent deformation may be described by the elastic-secondary creep constitutive relation

$$\dot{\varepsilon} = \dot{\sigma}/E + A\sigma^{n}, \tag{2.1}$$

where $\dot{\varepsilon}$ is the uniaxial strain rate, $\dot{\sigma}$ the uniaxial stress rate, E the Young's modulus, and A and n the steady-state creep coefficient and exponent, respectively.

A generalization of Equation 2.1 for multiaxial stress state is given by:

$$\dot{\varepsilon}'_{ij} = \frac{1+\nu}{E}\dot{\sigma}'_{ij} + \frac{3}{2}A\bar{\sigma}^{n-1}\sigma'_{ij}, \tag{2.2}$$

where $\dot{\varepsilon}'_{ij}$ and σ'_{ij} are deviatoric components of strain rate and stress and ν is Poisson's ratio. The effective stress defined by

$$\bar{\sigma} = \left(\frac{3}{2}\sigma'_{ij}\sigma'_{ij}\right)^{1/2}. \tag{2.3}$$

The constitutive relations (2.1)–(2.3) are available in the finite element code ABAQUS [11]. The uniaxial relation between the steady-state creep rate $\dot{\varepsilon}_{cr}$ and the stress σ is shown in Fig. 1. The material constants A and n were obtained from the creep test data at 650, 700 and 750°C, using a least-square method. Material constants at 725°C were obtained from an interpolation based on the results obtained at 650, 700 and 750°C, as shown in Table I.

Time-independent plasticity is described using von Mises yield surface with an isotropic hardening rule. Uniaxial tensile test data were used to obtain the relationship between the plastic strain and the stress at 650°C, as shown in Fig. 2. This relationship was then used in ABAQUS to model the time-independent plasticity. Since there are no test data available for temperature over 650°C, plasticity was considered only at 650°C.

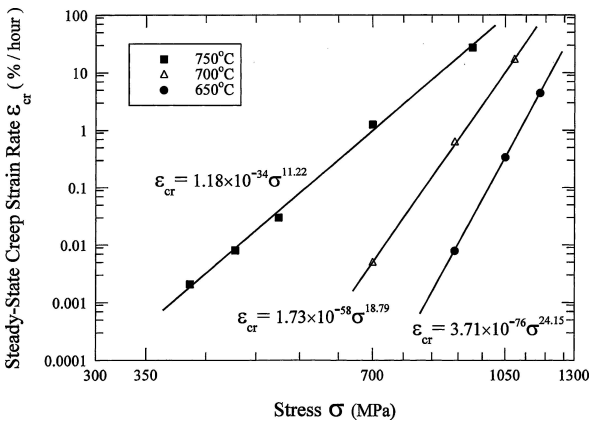

Figure 1 Uniaxial relation between the steady-state creep rate $\dot{\varepsilon}_{cr}$ and the applied stress σ for Alloy X at 650, 700 and 750°C, respectively.

TABLE I Material constants of Alloy X at 650, 700 and 750°C

Temperature (°C)	E(GPa)	ν	A (MPa^{-n}/h)	n
650	190	0.285	3.71×10^{-76}	24.15
700	181	0.290	1.73×10^{-58}	18.79
750	176	0.296	1.18×10^{-34}	11.22

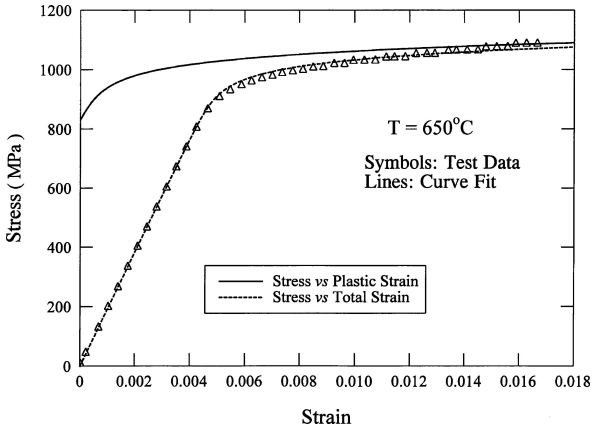

Figure 2 The stress versus strain curve under monotonic tensile loading.

2.1.2. Finite element models

Crack growth in a standard side-grooved compact tension (CT) specimen (width = 26 mm and effective thickness = 11.56 mm) was modelled using ABAQUS [11]. The mesh used for the analysis consists of 3098 four-noded plane-strain isoparametric elements, as shown in Fig. 3, where an extremely dense mesh ($\Delta/a = 3.9 \times 10^{-3}$) was generated around the crack growth area. Eight-noded quadratic elements with reduced integration would normally be the first choice for the analysis of stationary plastic/creep fracture mechanics, since the crack tip singularities can be properly simulated and a less refined mesh is required. However, for crack propagation analysis, four-noded first-order elements are recommended [11]. Only the upper half of the specimen was considered due to the symmetry. A load of $P = 7$ kN was applied to a rigid pin constructed to fit the hole, as shown in the mesh. The rigid pin and the specimen were modelled as contact surfaces. Crack growth was simulated by releasing a sequence of 64 nodes along the lower boundary of the dense portion of the mesh. A rigid surface was introduced along the symmetry axis. The 64 nodes were bonded to the rigid surface and they were allowed to slide along the rigid surface before the start of crack growth. A criterion of crack length versus time obtained experimentally (Fig. 4) was used to control the crack growth procedure, i.e., the debonding of the 64 nodes from the rigid surface.

As the crack grows from one nodal position to the next, the force carried by the node is gradually released

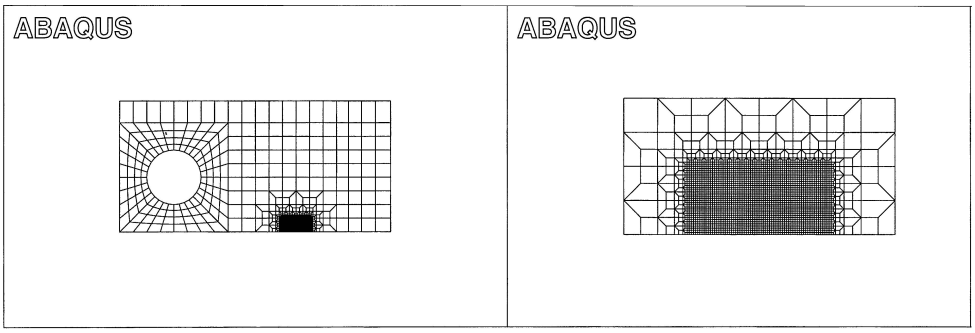

Figure 3 The finite element mesh used for the creep analysis: (a) the model and (b) the refined mesh around the crack growth area ($\Delta/a = 3.9 \times 10^{-3}$).

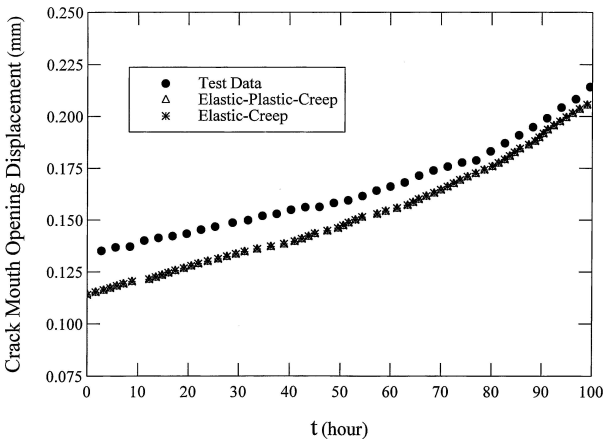

Figure 4 Comparison of the measured crack mouth opening displacement with that obtained from the finite element analysis at 650°C.

over a number of time increments. To keep the crack open during the crack growth, the rate of force release was chosen to be faster than the rate of force relaxation caused by plasticity/creep deformation. Specifically in our work, the relative amplitude of the force carried by the node is 1.0 at time $t = t_0$, 0.96 at $t - t_0 = 10^{-14}$ h, and then reduces to 0 as a linear function of log $(t - t_0)$. Here, t_0 is the time at which the node starts to debond from the rigid surface. The variation of the time increment during the plastic/creep analysis was automatically selected by ABAQUS after giving the value of the reference parameter CETOL [11] that controls the accuracy of the analysis. For our case, the value of CETOL was chosen to be 1.0×10^{-4} and this allows about 1% relative error in the estimated stress near the crack tip. The minimum time increment, adopted in ABAQUS just after the debonding of a node, was as small as 10^{-14} h to ensure convergence. This numerical procedure has been successfully applied in our previous work [12] to simulate constant creep crack growth in a conventional nickel-based superalloy, Waspaloy. The finite element model and the numerical procedure were adopted for both elastic-creep (EC) and elastic-plastic-creep (EPC) simulations.

2.2. Results and discussion

The crack mouth opening displacement was recorded on the crack face using an extensometer during the experiment. Both EC and EPC models were used to obtain the same quantity at the exact position as in the experiment. Fig. 4 shows the comparison of the results from the experiment and the simulation at 650°C. The general agreement seems to be reasonable, with the maximum error of about 15% occurred during the initial period. The results from the EC and EPC models are almost identical, indicating the insensitivity of the far field displacement response to the addition of classical plasticity. Fig. 5 shows the components of the load-line displacement (a) and the load-line displacement rate (b). The elastic displacement was obtained as a function of crack length from an elastic analysis [13]; while the displacement due to creep was obtained

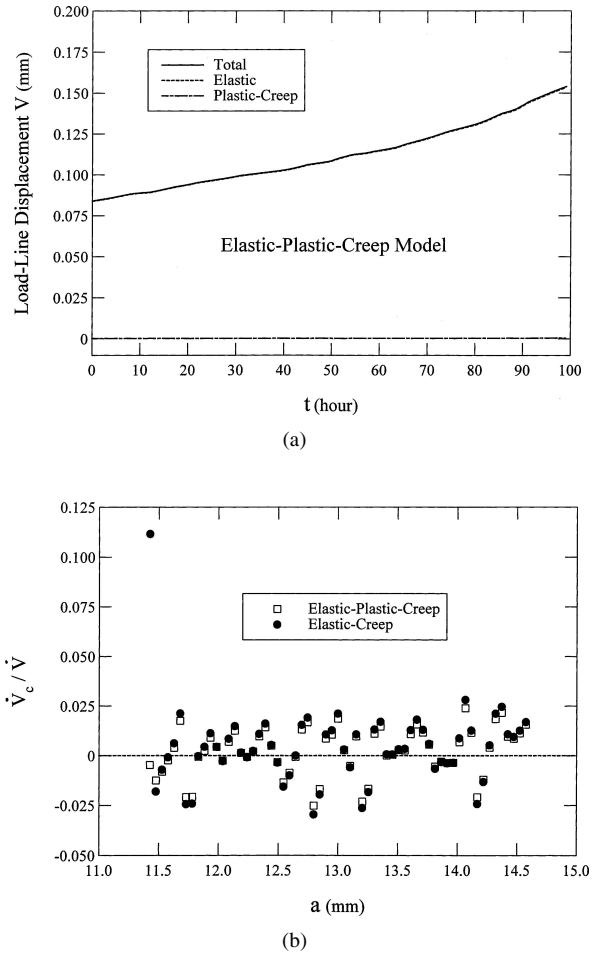

Figure 5 (a) The load-line displacement obtained from the elastic-plastic-creep model. (b) The ratio of creep/plastic deflection rate ($\dot{V}_C$) to total deflection rate ($\dot{V}$) against the crack length.

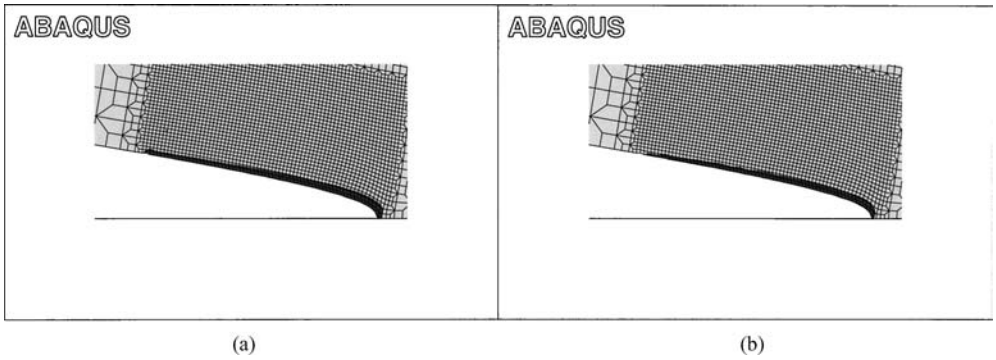

Figure 6 The plastic zone (a) and the creep zone (b) left in the wake of the crack growth from the elastic-plastic-creep (EPC) model.

by removing the elastic component from the total deflection. The associated displacement rates were obtained subsequently using a secant method [6]. Again, both EPC and EC models reveal the same pattern of load-line displacements with the displacement almost entirely attributes to elastic deformation. The ratio of displacement rates $\dot{V}_C/\dot{V}$ seem to oscillate around zero and in all cases, $\dot{V}_C/\dot{V} \ll 1$ applies. This indicates that the material is essentially creep-brittle and the creep deformation developed during the crack growth is negligible.

The evolution of plastic and creep zone was evaluated by defining the locus of the data points where the effective inelastic or creep strain ($\bar{\varepsilon}_{in}/\bar{\varepsilon}_{cr}$) is equal to the effective elastic strain $\bar{\varepsilon}_e$. Fig. 6 shows the contour plots of the inelastic strain (a) and creep strain (b). The filled dark areas represent the inelastic (a) and creep (b) zones. Clearly, both deformation seems to be confined to a thin layer adjacent to the crack growth path. Fig. 7 shows the combined creep-plastic zone left in the wake of the crack path as well as the creep and plastic components in the vertical (90°) direction. While the plastic zone seems to increase with the increase of crack length, the development of the creep zone seems to be only weakly correlated with the crack length. It is interesting to note, however, that the creep zones from the EC model are almost identical to those of plastic-creep zones obtained from the EPC model (Fig. 8). This is due to the unique characteristic of the HR field where the near tip stress amplitude is soly determined by the crack growth rate and independent of the load

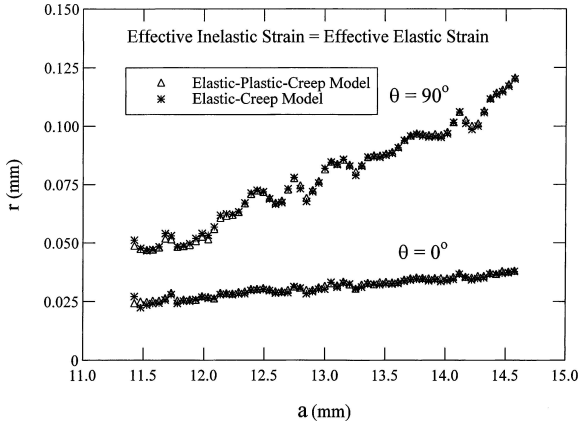

Figure 8 The radii of the creep/plastic zone along the $\theta = 0°$ and $\theta = 90°$ direction, comparison of EPC and EC models.

and crack growth history. Consequently, by ignoring the time-independent plasticity, the elastic-creep model may overestimate the creep deformation.

Fig. 9 shows the profiles of the effective stress near the crack tip in the vertical direction from the EPC model. Stress relaxation at the early stage was insignificant and HR field gained dominance almost instantly. The amplitude of the effective stress near the crack tip is slightly higher (10%) in EPC case than that in EC case (omitted for clarity), possibly due to the isotropic hardening introduced in the EPC model. The creep/plastic zones are nevertheless identical in both cases.

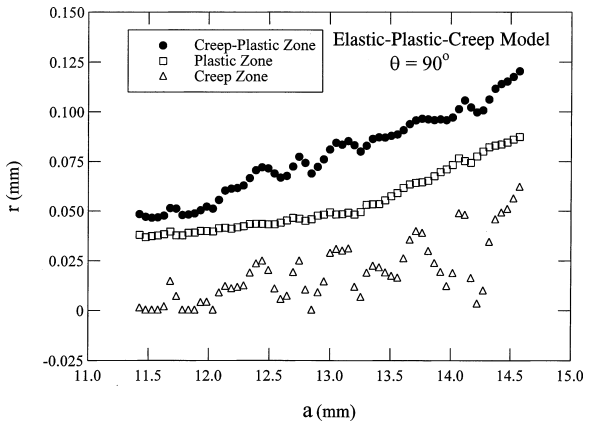

Figure 7 The radii of the creep and plastic zone in the crack wake along the $\theta = 90°$ direction, EPC model.

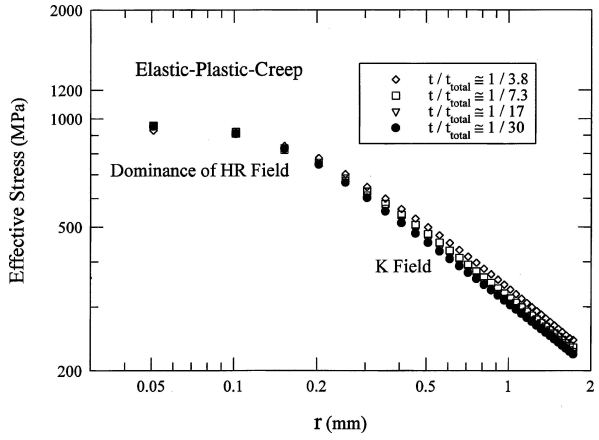

Figure 9 Effective stresses $\bar{\sigma}$ near the crack tip along the $\theta = 90°$ direction for the elastic-plastic-creep model.

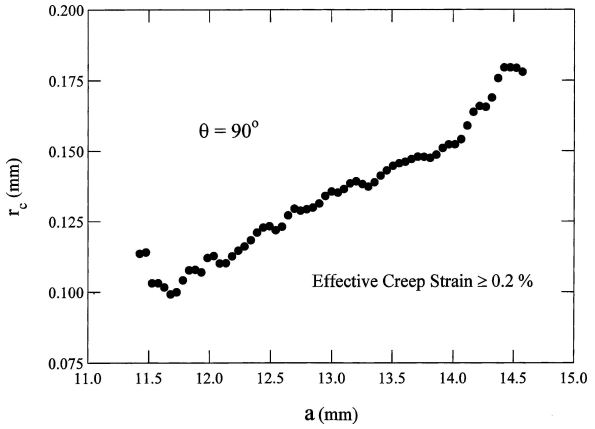

Figure 10 The radii of the creep zone in the wake of crack growth along the $\theta = 90^\circ$ direction at 725°C.

At 725°C, the results from the finite element analysis are very similar to those obtained at 650°C. Fig. 10 shows the creep zone left in the wake of crack growth. The distribution of the effective stress near the crack tip is very similar to that at 650°C, omitted here for space consideration. The creep deformation measured using displacement/displacement rate was again very limited (omitted) and the overall crack growth pattern unchanged, albeit a slight increase in the size of the creep zone (Figs 8 and 10).

3. Modelling of crack growth under cyclic load

3.1. The constitutive model

An elastic-plastic constitutive model has been used in this work to describe the time-independent crack growth under cyclic loads. Both isotropic and kinematic hardening have been considered in the cyclic stress strain behaviour. For small strain deformation, the strain tensor ε may be partitioned into an elastic part ε_e and a plastic part ε_p:

$$\varepsilon = \varepsilon_e + \varepsilon_p \tag{3.1}$$

According to the von Mises yield criterion, the yield function f is defined as

$$f(\sigma, \chi, R, k) = J(\sigma - \chi) - R - k \leq 0 \tag{3.2}$$

where χ is the kinematic hardening variable, R is the isotropic hardening variable and k is the initial value of the radius of the yield surface. J denotes the von Mises distance in the deviatoric stress space

$$J(\sigma - \chi) = \sqrt{\frac{3}{2}(\sigma' - \chi') : (\sigma' - \chi')} \tag{3.3}$$

where σ' and χ' are the deviators of σ and χ; while: represents the inner product of two tensors.

The evolution of the kinematic stress tensor χ and the isotropic stress R may be described through the following rules [14]

$$\dot{\chi} = \frac{2}{3} C \dot{\varepsilon}_p - \gamma \chi \dot{p} \quad \text{and} \quad \dot{R} = b(Q - R)\dot{p} \tag{3.4}$$

TABLE II Optimized parameters for the constitutive equation

E (GPa)	k (MPa)	Q (MPa)	b	C (GPa)	γ
205	600	150	6.8	540	1200

where C, γ, b and Q are four material and temperature dependent constants which determine the shape and amplitude of the stress-strain loops during the transient and saturated stage of cyclic response.

The above constitutive equations are available in ABAQUS. The six material parameters, E, k, b, Q, C and γ, are optimized from the uniaxial test data of Alloy X at the temperature of 300°C [15], as shown in Table II. The choice of this temperature is to ensure pure time-independent deformation during crack growth as opposed to the cases studied in Section 2.

3.2. Finite element model

Fatigue crack growth in a CT specimen was simulated using the full constitutive model as detailed in 3.1. A total crack growth of 1.6 mm was simulated with an initial length of 12.2 mm and a final crack length of 13.8 mm. The element size in the crack growth area is 12.7 μm, sufficient for the purpose of crack growth modeling where the forward plastic zone would contain about 27 elements. Four-noded first-order elements with full integration were used as they are preferred for crack propagation analysis [11]. The maximum applied cyclic load was 7 kN with a load ratio R chosen to be zero. The limit load, P_0, at the initial crack length is 27.5 kN for plane strain ($P_{max}/P_0 = 0.25$) and 20.2 kN for plane stress ($P_{max}/P_0 = 0.35$). Again, the load was applied to a rigid pin fitted into the hole of the specimen. The rigid pin and the specimen were treated as contact surfaces. The crack growth was simulated by releasing a sequence of nodes along the path of crack growth. The nodes to be released were initially bonded to a rigid surface introduced along the symmetry axis. The bonded nodes were allowed to slide along the rigid surface before the start of crack growth. A criterion of crack length versus time [15] was used to control the crack growth procedure, i.e., the debonding of the nodes from the rigid surface and the node was released just after reaching the maximum load. The first cycle was used to allow the stabilization of the stress-strain curve around the crack tip. The crack closure was examined at the minimum load of the second cycle. As the crack grew from one nodal position to the next, the force carried by the node was gradually released to zero over a half cycle. Specifically in our work, the relative amplitude of the force carried by the node was 1.0 at the start of node debonding and reduced to 0 as a linear function of the time in a half cycle. The adopted time increment was the same as that used in the analysis for a stationary fatigue crack, i.e, 160 increments for each cycle. Contact elements were built up between the crack surface and a rigid surface constructed along the symmetry axis to prevent the overlap of crack surfaces during unloading. A total of 256 cycles were required, representing an average crack growth rate of 6.25×10^{-6} m/cycle. In addition to plane stress and plane strain conditions, a generalized plane strain [11]

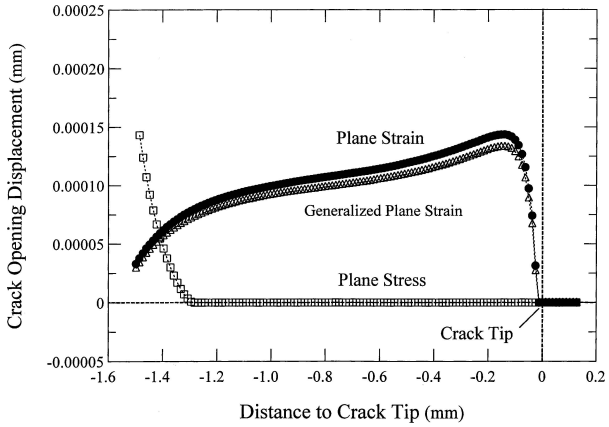

Figure 11 Crack opening profiles at the minimum load ($a_f = 13.8$ mm) for plane strain, generalised plane strain and plane stress conditions.

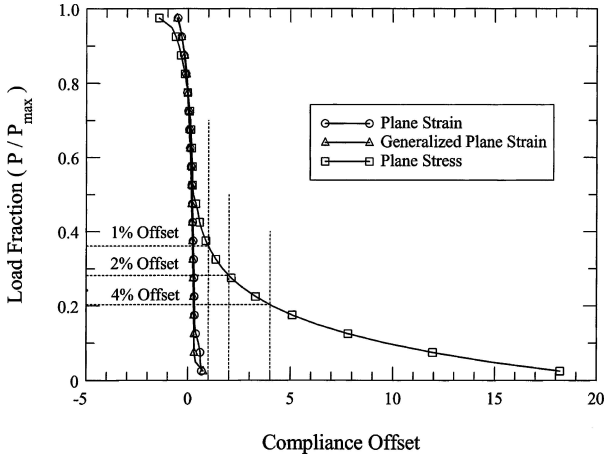

Figure 12 The load-complaince offset plot at $a_f = 13.8$ mm for plane strain, generalised plane strain and plane stress conditions.

condition was also considered to allow the deformation in the thickness direction and hence more representative of real specimens.

3.3. Results and discussion

The crack opening profiles following a crack growth of 1.6 mm are shown in Fig. 11 for plane stress, plane strain and generalized plane strain conditions. For plane strain and generalized plane strain conditions, the crack stays open except the first element next to the crack tip, suggesting no physical closure at the minimum load. This is consistent with the work by Fleck and Newman [17] who reported crack closure over one element in a plane-strain bend specimen. Fleck and Newman [17] reported that the crack closure was associated with the transient crack growth ($\Delta a < 0.5$ mm) and decayed steadily towards steady-state crack growth. This may help to explain the difference in the crack closure behaviour when the length of crack growth differs, as reported in [17]. The closure behaviour observed under generalized plane strain condition seems to be similar to that under plane strain, and physical closure is absent in both cases.

Substantial crack closure (1.26 mm contact length for 1.6 mm crack growth) was observed under plane stress condition, consistent with numerous experimental and finite element studies. Compliance measurements using displacement or strain gauges have previously been used to assess crack closure. Fleck [19] reported $U = 0.72$ for a CT specimen in the plane stress condition measured using four different experimental methods. This level of crack opening compares well with the current study, where $U = 0.72$ is obtained from 0.2% of the load-displacement offset trace (Fig. 12). In finite element analysis, crack closure is often evaluated by directly monitoring the displacements of the nodes on the crack surface during unloading. Crack closure is assumed when a zero normal displacement is recorded at the first or preferably the second node behind the crack tip. The second node was monitored in this work. The obtained opening level U is about 0.57. Clearly, the level of crack opening differs considerably from different methods of evaluation.

The significance of crack closure in modifying the effective stress intensity factor range has been examined. For the plane stress condition, the stress intensity factor K at the final crack length ($a_f = 13.8$ mm) was determined using a displacement method [12] under small scale yielding conditions. The range of K-dominant field was identified and selected nodes away from the crack tip and the crack growth area were used to plot the apparent stress intensity as a function of r for $\theta = 180°$, based on the displacement output from the FE model. The K value at the crack tip ($r = 0$) was then extrapolated from the apparent stress intensity versus r curve. The calculation was repeated for a whole loading cycle. The obtained solution is compared with the standard CT solution in Fig. 13, where the crack opening range observed during the FE simulation is also indicated. Clearly the stress intensity factor range during the crack opening period does not coincide with the actual stress intensity factor range obtained by the displacement method (marked as FE solution). The FE solution gives a stress intensity factor range of 32.1 MPa$\sqrt{\text{m}}$, compared with the "effective" stress intensity range of 25.6 MPa$\sqrt{\text{m}}$ from the compliance analysis and 20.3 MPa$\sqrt{\text{m}}$ indicated by the physical "opening" of the crack. These results seem to cast some doubts on the validity of the current practice in crack closure measurement. The compliance approach

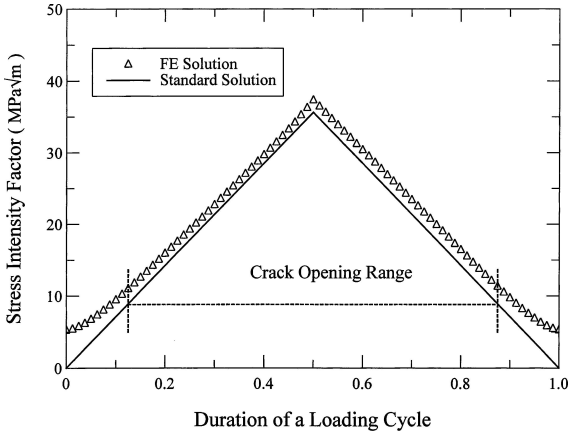

Figure 13 Variation of the stress intensity factor during a loading cycle at $a_f = 13.8$ mm for plane stress conmdition; comparison of the finite element and standard elastic solutions.

seems to have exaggerated the role of crack closure with a 28% reduction in nominal stress intensity range compared with a 10% reduction from the FE analysis.

4. Concluding remarks

The finite element method has been used to model the time-dependent crack growth under sustained loads and the time-independent fatigue crack growth. Elastic-creep and elastic-plastic-creep models have been used to simulate the crack growth under sustained loads while a constitutive model with both kinematic and isotropic hardening deformation has been used in the simulation of fatigue crack.

Creep damage was found to be very limited at both temperatures considered. This would suggest a "creep-brittle" characteristic in Alloy X that seems to warrant an elastic parameter, such as stress intensity factor K, as a characterization parameter. For fatigue crack growth, the norminal stress intensity factor K would seem to suffice for plane strain or generalised plane strain loading conditions. Even for plane stress conditions, the role of crack closure seems to be only marginal.

Acknowledgements

This work was supported by the Engineering and Physical Science Research Council (EPSRC) of UK (GR/M44811).

References

1. S. DALBY and J. TONG, *J. Mater. Sci.*, Part I of this paper.
2. J. W. HUTCHINSON, *J. Mech. Phys. Solids* **16** (1968) 13.
3. H. RIEDEL and J. R. RICE, "ASTM STP700" (1980) p. 112.
4. A. SAXENA, D. E. HALL and D. L. McDOWELL, *Engng. Fract. Mech.* **62** (1999) 111.
5. A. SAXENA, "ASTM STP905" (1986) p. 185.
6. ASTME1457-92, ASTM, 1992.
7. M. C. HARDY, private communication, 1999.
8. S. POMMIER, C. PRIOUL and P. BOMPARD, *Fatigue Fract. Engng. Mater. Struc.* **20** (1997) 93.
9. S. POMMIER and P. BOMPARD, *ibid.* **23** (2000) 129.
10. S. POMMIER, *Eng. Fract. Mech.* **69** (2002) 25.
11. ABAQUS 5.8, Hibbitt, Karlsson & Sorensen, Inc.
12. L.-G. ZHAO, J. TONG and J. BYRNE, *Eng. Fract. Mech.* **68** (2001) 1157.
13. T. L. ANDERSON, "Fracture Mechanics: Fundamentals and Applications" (CRC Press, 1995).
14. J.-L. CHABOCHE, *Int J Plasticity* **2** (1986) 149.
15. L.-G. ZHAO, J TONG and J. BYRNE, *Mech. Mater.* **33** (2001) 593.
16. R. C. McCLUNG, B. H. THACKER and S. TOY, *Int J Fracture* **50** (1991) 27.
17. N. A. FLECK and J. C. NEWMAN, ASTM STP987 (1988) p. 319.
18. H. SEHITOGLU and W. SUN, *ASME J Eng Mater. Tech.* **113** (1991) 31.
19. N. A. FLECK, "Fatigue Crack Measurement: Techniques and Applications, edited by K. J. Marsh, R. A. Smith and R. O. Ritchie (EMAS, 1991).
20. R. C. McCLUNG and H. SEHITOGLU, *Eng. Fract. Mech.* **33** (1989) 237.

Received 8 October 2003
and accepted 24 September 2004